




# INTEGRATION OF GEOCHEMISTRY INTO A GEOMECHANICAL SUBSURFACE FLOW SIMULATOR

Miki Mura<sup>1</sup> , Shuang Zheng<sup>2,3</sup> , Mukul M. Sharma<sup>1</sup> 

<sup>1</sup>Department of Petroleum Engineering, The University of Texas at Austin, Austin, Texas, USA; <sup>2</sup>Previous: Department of Petroleum Engineering, The University of Texas at Austin, Austin, Texas, USA; <sup>3</sup>Current: Aramco Americas, Houston, Texas, USA

## Correspondence to:

Miki Mura,  
[miki.mura@austin.utexas.edu](mailto:miki.mura@austin.utexas.edu)

## How to Cite:

Mura, M., Zheng, S., & Sharma, M. Integration of Geochemistry into a Geomechanical Subsurface Flow Simulator. *InterPore Journal*, 1(3), IPJ271124–4.  
<https://doi.org/10.69631/ipj.v1i3nr6>

RECEIVED: 13 Aug. 2023

ACCEPTED: 11 Sept. 2024

PUBLISHED: 27 Nov. 2024

## ABSTRACT

Accurately modeling geochemical reactions in subsurface flow is essential for understanding processes such as CO<sub>2</sub> sequestration and contaminant transport. This paper presents a new numerical subsurface simulator (MF3D-GC) that combines flow, geomechanics, and geochemistry in an integrated and fully coupled manner. The simulator's capabilities were benchmarked by comparing it with other reactive-transport simulators. An adaptive tolerance method was implemented in the geochemistry module which reduced computing time while maintaining accuracy. User-defined kinetic models were used and coupled with changes in specific surface area, fluid saturation, temperature, and pH. The unique abilities of the model to couple geomechanics with geochemistry are highlighted. Our results show the importance of carefully selecting minerals and models to balance accuracy and computational efficiency. The model is used to simulate six different classes of geochemical flow problems which include flow, dissolution, precipitation, redox reactions, and diffusion with increasing levels of complexity. The potential applications of the model to CO<sub>2</sub> sequestration, solution mining, geothermal energy production, and contaminant transport are briefly discussed.

## KEYWORDS

Reactive Transport Modeling, Geomechanics, Fractured Reservoir, CCUS, CO<sub>2</sub> capture, utilization, and storage



@2024 The Authors

This is an open access article published by InterPore under the terms of the Creative Commons Attribution-NonCommercial-NoDerivatives 4.0 International License (CC BY-NC-ND 4.0) (<https://creativecommons.org/licenses/by-nc-nd/4.0/>).

## 1. INTRODUCTION

The growing demand to reduce greenhouse gases has intensified efforts to combat global climate change. Scientists and engineers have advanced CO<sub>2</sub> capture, utilization, and storage (CCUS) technologies through lab experiments and simulations, establishing CCUS as a promising method for reducing CO<sub>2</sub> emissions. Several commercial-scale CCUS projects are emerging after successful pilot projects. Assessing risks, ensuring injection well capacity, and maintaining fluid confinement in geological formations throughout a project's lifespan are crucial for project success.

Injecting large volumes of CO<sub>2</sub> over extended periods involves the coupling of hydrology, geochemistry, and geomechanics. Changes in stress and strain with temperature and pressure fluctuations can affect both short-term and long-term performance, leading to deformation and seismic events (27, 32). For example, uplifts in the Salah CO<sub>2</sub> storage project in Algeria suggest hydraulic fracturing in reservoir and cap rocks (32, 45). Studies have examined CO<sub>2</sub> sequestration safety by analyzing fault reactivation and seismic events (10, 19).

As previously stated, CO<sub>2</sub> injection includes the coupling of hydrology and geochemistry, as the acidity of formation water leads to the dissolution of primary minerals and precipitation of secondary minerals, resulting in a stable form of subsurface CO<sub>2</sub> storage (e.g., 3, 23, 42, 47). The CarbFix2 project in Iceland observed mineralization of carbonates and sulfates after injecting CO<sub>2</sub> and H<sub>2</sub>S into basalts. Additionally, geomechanics and geochemistry interact, altering flow and mechanical properties over time. Therefore, fully coupled geochemical models accounting for geomechanical changes are essential, as CO<sub>2</sub> injection leads to complex physical and chemical processes.

Numerous numerical simulators have been developed to investigate the geomechanical and chemical interaction of CO<sub>2</sub> with subsurface minerals (1, 32). These simulators fall into three categories based on their coupling capabilities:

1. **Geomechanics and Hydrology:** Examples include TOUGH-FLAC (31), OpenGeoSys (9), CODE-BRIGHT (25), ECLIPSE-VISAGE (26), STARS (2, 7).
2. **Reactive-Transport (Hydrology and Geochemistry):** Examples include TOUGHREACT (48), PHREEQC (29), MIN3P (21), and UTCHEM (13, 43).
3. **Fully Integrated (Hydrology, Geomechanics, and Geochemistry):** Examples include TOUGHREACT linked with FLAC3D (33, 41), or Retraso linked with CodeBright (15).

Despite their advancements, these simulators have limitations. Models that include geomechanics and geochemistry simplify the flow problem to one-dimensional (1D), single phase flow.

This study aims to develop and test a fully 3D, coupled geomechanics and geochemistry simulator by incorporating geochemical capabilities into the geomechanics-based simulator Multi-frac 3D (MF3D), a fully integrated multi-phase, equation of state compositional hydraulic fracturing and subsurface simulator (50). PhreeqcRM (30) and porousMedia4Foam (36) provide geochemical capabilities. PhreeqcRM includes a geochemistry reaction module for PHREEQC (29), while porousMedia4Foam connect PhreeqcRM with any flow simulator available on the OpenFOAM® Platform (44). This work showcases the successful integration of these models into a single, fully-coupled system focusing on the single-phase aspect. The primary goal is to study CO<sub>2</sub> sequestration projects, but the versatility of our new model (MF3D-GC) extends its applicability to fields like solution mining and geothermal energy production.

## 2. MODEL DESCRIPTION

The proposed work aims to build an integrated 3D subsurface model with non-isothermal, single phase flow, geomechanics and geochemical capabilities. To accomplish this, the general flow-geomechanics simulator (MF3D) is integrated with the geochemistry library PHREEQC (29). PHREEQC is widely used for simulating chemical reactions in aqueous systems, however it is limited to only 1D flow and lacks geomechanics. The new model (MF3D-GC) can now model chemical reactions in both aqueous and solid phases within geological formation, including intra-aqueous, mineral dissolution and precipitation, adsorption, and redox reactions.

MF3D-GC can model CO<sub>2</sub> injection scenarios, where CO<sub>2</sub> lowers the pH of the formation water, leading to mineral dissolution. The geochemistry module can capture these reactions, while changes in porosity affect permeability and pressure distribution. Pressure changes can also impact the subsurface stress state. Capturing all these coupled effects provides a more accurate representation of subsurface physical behavior resulting from CO<sub>2</sub> injection.

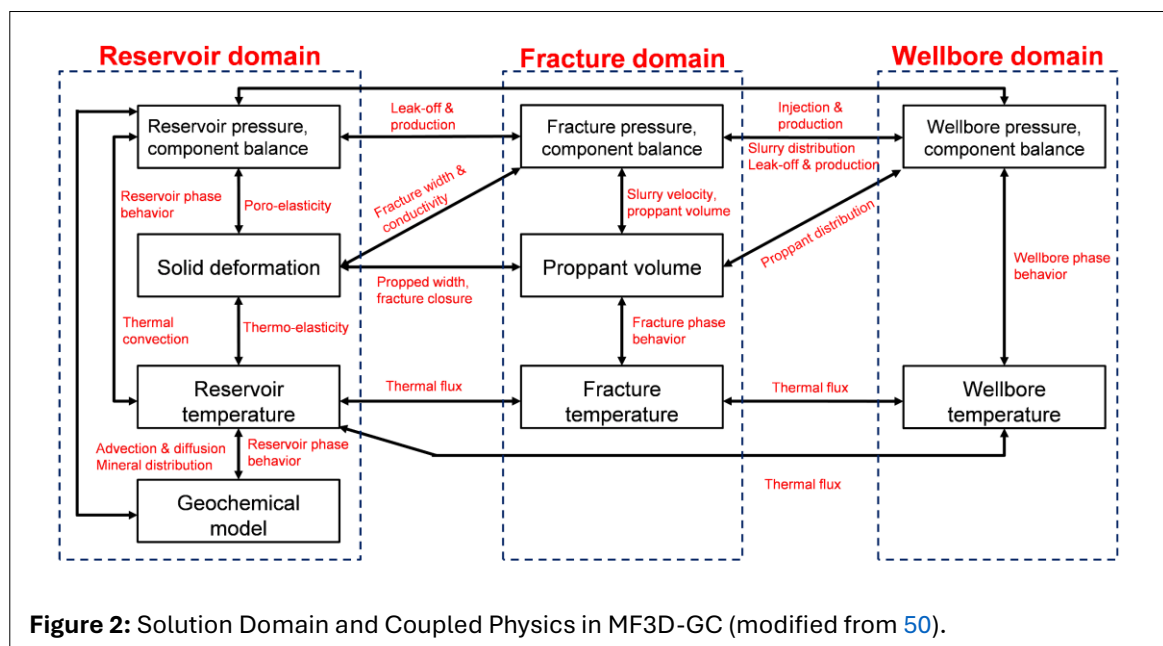
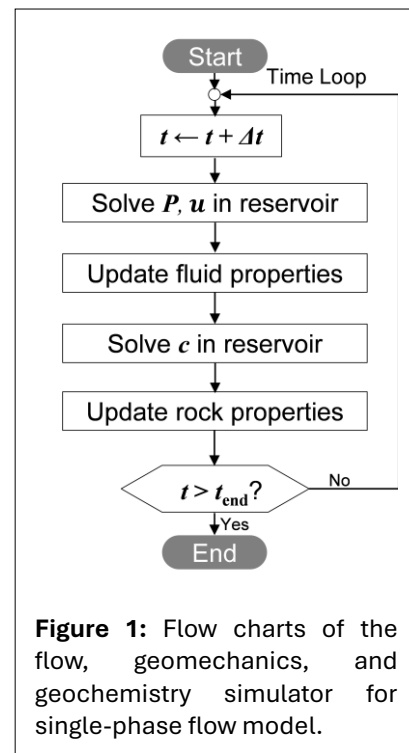
The subsurface simulation process (Fig. 1) involves the implicit calculation of pressure and deformation in the reservoir domain at each time step. Fluid properties are updated based on pressure, and the geochemistry module explicitly solves for the aqueous species concentration and reactive mineral volume. After the geochemical reactions are solved, the simulator updates rock properties based on mineral volume and proceeds to the next timestep. This process integrates reservoir flow, geomechanics, and geochemistry.

The integration of MF3D and PHREEQC was facilitated by C++ packages, PhreeqcRM (30) and porousMedia4Foam (36). PhreeqcRM allows easy access to PHREEQC's reaction capabilities from existing multicomponent transport simulators, while porousMedia4Foam extends the accessibility to PHREEQC using PhreeqcRM for flow transport simulators on the OpenFOAM® platform, a C++ toolbox for numerical solver development. MF3D also uses OpenFOAM® to address fracture propagation and fluid flow in reservoirs (50), enabling the seamless adaptation of porousMedia4Foam to MF3D.

The MF3D-GC code consists of three interconnected modules: the flow and geomechanics solver (MF3D; Section 2.1); the reactive transport solver (modified porousMedia4Foam; Section 2.2); and the flow and rock properties alteration module, which accounts for the interaction of geomechanics and geochemistry (Section 2.3). While MF3D offers versatile geomechanical capabilities to simulate fracture propagation and wellbore deformation (Fig. 2), this work primarily focuses on the reservoir domain and the single-phase model. This paper aims to introduce the models used to implement the interactions between flow, geomechanics, and geochemistry in an integrated manner (Fig. 2).

## 2.1. Fluid Flow and Geomechanics Modeling

MF3D solves fluid flow and geomechanics implicitly on a reservoir scale. Jasak and Weller discussed the benefits of using the finite volume method (FVM) for linear elasticity in OpenFOAM® (12). Tang expanded this by introducing a poro-elasto-plastic model in OpenFOAM® (39, 40). Manchanda further extended this concept for hydraulic fracturing, developing a hydraulic fracture and reservoir simulator (20). The latest MF3D version employs a block-coupled FVM (5) to enhance computational efficiency



(50). MF3D simultaneously solves governing equations for fluid flow (Section 2.1.1) and geomechanics (Section 2.1.2) in a poro-elastic medium within the reservoir domain.

### 2.1.1. Fluid Flow in Poro-Elastic Medium

Fluid flow in a poro-elastic medium is derived from a continuity equation for the fluid (8, 20, 50). In single-phase state (Eq. 1), where  $\phi$  is the porosity,  $t$  is time, and  $\mathbf{q}_w$  is the water flux vector in a 3D Cartesian coordination system.

$$\frac{\partial \phi}{\partial t} + \nabla \cdot \mathbf{q}_w = 0 \quad (1)$$

The water flux  $\mathbf{q}_w$  is described by Darcy's law (Eq. 2):

$$\mathbf{q} = -\frac{\mathbf{k}_m}{\mu_w} (\nabla p - \rho_w \mathbf{g} \nabla D) \quad (2)$$

where  $\mathbf{k}_m$  is the matrix permeability tensor,  $\mu_w$  is the water viscosity,  $p$  is pore pressure,  $\rho_w$  is the water density, and  $\mathbf{g}$  is gravitational force vector. In the poro-elastic medium, the constitutive equation for pore pressure is (Eq. 3):

$$p = M(\phi - \alpha \varepsilon_b) = M\{\phi - \alpha(\nabla \mathbf{u})\} \quad (3)$$

where  $M$  is Biot's modulus,  $\alpha$  is Biot's effective stress coefficient,  $\varepsilon_b$  is the bulk volumetric strain and  $\mathbf{u}$  is the total displacement vector (11). Combining these models, fluid flow in a poro-elastic medium is described as (Eq. 4):

$$\frac{\partial p}{\partial t} = \nabla \cdot \left( \frac{\mathbf{k}_m M}{\mu_w} \nabla p \right) - \alpha M \frac{\partial}{\partial t} (\nabla \mathbf{u}) - \nabla \cdot \left( \frac{\mathbf{k}_m M}{\mu_w} \rho_w \mathbf{g} \nabla D \right) \quad (4)$$

Accordingly, the governing equation for single-phase fluid flow in a poro-elastic medium is obtained as shown in Equation 5 where  $\Omega$  is the control volume.

$$\int_{\Omega} \frac{1}{M} \frac{dp}{dt} d\Omega = \int_{\Omega} \nabla \cdot \left( \frac{\mathbf{k}_m}{\mu_w} \nabla p \right) d\Omega - \int_{\Omega} \alpha \frac{\partial}{\partial t} (\nabla \mathbf{u}) d\Omega - \int_{\Omega} \nabla \cdot \left( \frac{\mathbf{k}_m}{\mu_w} \rho_w \mathbf{g} \nabla D \right) d\Omega \quad (5)$$

### 2.1.2. Coupling Flow and Geomechanics in a Poro-Elastic Medium

The poro-elastic deformation equation in the reservoir is derived from the condition for mechanical equilibrium (Eq. 6), where  $\boldsymbol{\sigma}$  is the Cauchy stress tensor, and  $\mathbf{F}$  is the body force vector per unit volume of the bulk material (11).

$$\nabla \cdot \boldsymbol{\sigma} = -\mathbf{F} \quad (6)$$

Cardiff (5) introduced a block-coupled FVM for conserving linear momentum within an arbitrary body, neglecting inertia and body forces. For a volume  $\Omega$  bounded by surface  $\Gamma$ , the conservation of linear momentum is shown in Equation 7 where  $\mathbf{n}$  is the outward-facing unit normal.

$$\int_{\Omega} \nabla \cdot \boldsymbol{\sigma} d\Omega = \oint_{\Gamma} \mathbf{n} \cdot \boldsymbol{\sigma} d\Gamma = 0 \quad (7)$$

Using Hooke's Law and Biot's poro-elastic framework, the Cauchy stress tensor  $\boldsymbol{\sigma}$  for a linear elastic body is formulated as (Eq. 8):

$$\boldsymbol{\sigma} = \mu \nabla \mathbf{u} + \mu \nabla \mathbf{u}^T + \lambda \text{tr}(\nabla \mathbf{u}) \mathbf{I} + \boldsymbol{\sigma}_0 + \alpha p \mathbf{I} \quad (8)$$

where  $\mathbf{u}$  is the total displacement vector,  $\mu$  and  $\lambda$  are the Lamé coefficients,  $\boldsymbol{\sigma}_0$  is the in situ stress following a tension positive convention, and  $\alpha$  is Biot's effective stress coefficient, and  $\mathbf{I}$  is the identity matrix. Substituting  $\boldsymbol{\sigma}$  into the momentum conservation yields the governing equation for poro-elastic deformation (Eq. 9):

$$\oint_{\Gamma} \mathbf{n} \cdot [\mu \nabla \mathbf{u} + \mu \nabla \mathbf{u}^T + \lambda \text{tr}(\nabla \mathbf{u}) \mathbf{I} + \boldsymbol{\sigma}_0 + \alpha p \mathbf{I}] d\Gamma = 0 \quad (9)$$

MF3D fully couples geomechanics and fluid flow by introducing poro-elasticity and solving the coupled set flow and deformation equations implicitly (50). The displacement and pressure link the governing equations of fluid flow and geomechanics.

## 2.2. Reactive Transport Modeling

This section describes the governing equations and coupling method used in the reactive transport modeling part of MF3D-GC. The model MF3D-GC updates aqueous species concentration  $c_{iw}$  and mineral volume fractions  $Y_{s,i}$ , through reactive transport processes to achieve geochemical modeling capabilities.

This involves employing a reactive transport solver to address material balance equations for each chemical species  $i$ , thereby obtaining the concentration in the aqueous phase  $c_{iw}$  and the volume fraction of minerals  $Y_{s,i}$ . These equations are formulated as (Eq. 10):

$$\frac{\partial \mathbf{n}}{\partial t} + \nabla \cdot \mathbf{J}^s - \mathbf{S}_R - \mathbf{S}_{well} = \mathbf{0}_{N_s} \quad (10)$$

Here,  $\mathbf{n}$  represents the moles of chemical species per bulk volume,  $\mathbf{J}^s$  is the flux vector of species,  $\mathbf{S}_R$  is the vector of species supply/reduction rate due to reactions,  $\mathbf{S}_{well}$  is the species supply/withdrawal rates from wells, and  $N_s$  is the total number of chemical species (35). Each term can be specified for aqueous and mineral phases, as listed in Table 1.

Term	Symbol	Aqueous phase	Mineral Phase
Moles of chemical species	$n$	$\phi S_w c_{iw}$	$Y_{s,m} c_{im}$
Flux vector of species	$\mathbf{J}^s$	$u_w c_{iw}$ $- \phi S_w D_{iw} \nabla c_{iw}$	0
Vector of supply or reduction rate of chemical species due to chemical reactions	$\mathbf{S}_R$	$\sum_{q=1}^{N_Q} \widetilde{v}_{iq} R_q$ $+ \sum_{k=1}^{N_K} \widetilde{v}_{ik} R_k$	$\sum_{q=1}^{N_Q} \widetilde{v}_{iq} R_q$ $+ \sum_{k=1}^{N_K} \widetilde{v}_{ik} R_k$
Vector of supply or withdrawal rates of chemical species from the injector or producer wells	$\mathbf{S}_{well}$	$c_{i,well} q_{w,well}$	0

For the mineral phase  $m$ ,  $\mathbf{n}$  is given by solid volume fraction  $Y_{s,m}$  and concentration of chemical species  $i$  ( $c_{im}$ ). The flux  $\mathbf{J}^s$  exists only in the aqueous phase and includes advection and diffusion terms. The advection term uses the Darcy velocity  $u_w$ , introduced as  $\mathbf{q}_w$  in Equation 2, implicitly computed in the flow-geomechanics solver. The diffusion term involves the effective diffusion and dispersion tensor  $\mathbf{D}_{iw}$ , accounting for tortuosity and hydrodynamic dispersion.  $\mathbf{S}_R$  includes both equilibrium and kinetics reactions for aqueous and mineral phases. For equilibrium reactions ( $q$ ),  $\widetilde{v}_{iq}$  is the stoichiometric coefficient of species  $i$ , and  $R_q$  is the reaction rate, and  $N_Q$  is the total number of equilibrium reactions. Kinetic reactions ( $k$ ) are described by  $\widetilde{v}_{ik}$ ,  $R_k$ , and  $N_K$ . The well-related source term  $\mathbf{S}_{well}$ , which exists only in the aqueous phase, accounts for the species  $i$  concentration of the produced/injected water  $c_{i,well}$  and the injection /production rate  $q_{w,well}$ .

MF3D-GC solves the reactive transport model by splitting it into transport and reaction models. This methodology, known as Sequential Non-Iterative Approach (SNIA) (38), is discussed in Section 2.2.1. MF3D-GC also implements the adaptive tolerance approach (4) to reduce the computing time dedicated to the reactive transport solver, explained in Section 2.2.2.

### 2.2.1. Sequential Non-iterative Approach (SNIA)

MF3D-GC integrates MF3D with porousMedia4Foam and utilizes PhreeqcRM and PHREEQC. Both porousMedia4Foam and PhreeqcRM employ the sequential approach, also known as operator splitting approach, to solve the reactive transport equation (37). This includes Sequential Iterative Approach (SIA) and Sequential Non-Iterative Approach (SNIA) (38). Both methods solve transport and reaction models separately, but SIA iterates until convergence for more accuracy, while SNIA does not for numerical efficiency (48). MF3D-GC adopts SNIA by first calculating the transport part and then the reaction part, simplifying calculations and reducing computational cost.

### 2.2.2. Adaptive Tolerance Approach

While SNIA improves numerical efficiency, reactive transport simulators can still pose computational expenses due to numerous iterations in the geochemical module (24). MF3D-GC addresses this by implementing an adaptive tolerance approach (4), reducing chemical reaction calculations in each time step by ignoring geochemically inactive regions. This combination of SNIA and adaptive tolerance approach has effectively reduced computing time.

The adaptive tolerance approach is based on the reaction zone concept, which states that the geochemical module only needs to be called when there is a substantial change in the concentration of

any chemical species. In the cells far from the reaction zone, changes in species concentration from geochemical reactions  $S_R$  are negligible because the fluid is in equilibrium (34). This concept reduces the computational cost of reactive transport simulations, especially when advection dominates over other transport mechanisms (16).

The adaptive tolerance approach determines when and where to perform geochemical calculations by checking whether the relative molar concentration change  $c_r$ , obtained after solving the transport equation, exceeds the adaptive tolerance  $\epsilon$ . **Figure 3**

shows a flowchart of this process, which adjusts the criterion for executing geochemical calculations in response to the concentration change rate at each time step.

Specifically, the relative molar concentration change  $c_{r,i,j}^n$  in cell  $i$  for chemical component  $j$  at the  $n$ th (or time step) is formulated as **Equation 11**, where  $c_{i,j}^{stored}$  is the molar concentration in cell  $i$  for chemical component  $j$  at the most recent time step when the reactive calculation was performed at that cell.

$$c_{r,i,j}^n = 100 \times \left| \frac{c_{i,j}^n - c_{i,j}^{stored}}{c_{i,j}^{stored}} \right| \quad (11)$$

The adaptive tolerance  $\epsilon_{i,j}^n$ , at the  $n$ th timestep for cell  $i$  and chemical component  $j$ , is shown in **Equation 12**:

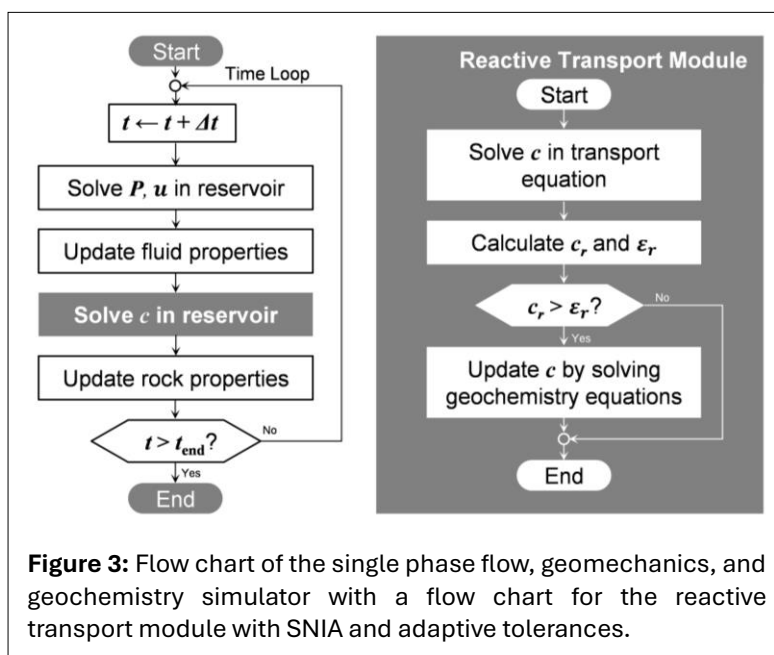


**Figure 3:** Flow chart of the single phase flow, geomechanics, and geochemistry simulator with a flow chart for the reactive transport module with SNIA and adaptive tolerances.

$$\varepsilon_{i,j}^{n+1} = \frac{1 + |\omega_{i,j}^{n-1}|}{1 + |\omega_{i,j}^n|} \cdot \varepsilon_{i,j}^n \quad (12)$$

Here,  $\omega_{i,j}^n$  and  $\omega_{i,j}^{n-1}$  are the normalized concentration slopes for cell  $i$  and chemical component  $j$  at  $n$ th and  $(n - 1)$ th timesteps (Eq. 13) where  $t$  is the simulation time.:

$$\omega_{i,j}^n = \frac{100}{c_{i,j}^n} \left( \frac{c_{i,j}^n - c_{i,j}^{n-1}}{t^n - t^{n-1}} \right) \quad (13)$$

This approach requires an initial adaptive tolerance  $\varepsilon_{i,j}^0$ , which defines the frequency of reactive calculations. Bordeaux-Rego recommends setting  $\varepsilon_{i,j}^0$  to 5% for reasonable accuracy and computing speed (4). In this work, the initial value  $\varepsilon_{i,j}^0$  is user-defined.

## 2.3. Flow Property Models

The reactive transport modeling in Section 2.2 incorporates a one-way coupling between flow and geochemistry using Darcy velocity and sink/source terms from wells. However, to fully account for geochemistry's impact on fluid flow, porosity and permeability can be added as coupling terms. This creates a fully integrated system that includes flow, geomechanics, and geochemistry in the simulator, with feedback between components. These integrations provide a more accurate representation of the dynamically evolving subsurface system.

### 2.3.1. Porosity

The solid volume fraction of a given mineral phase  $m$  in the controlled volume  $Y_{s,m}$  is determined through the material balance equations in mineral phases. The resulting porosity of the porous medium can then be computed using the following formula (Eq. 14) where  $Y_{s,inert}$  denotes the solid volume fraction of inert minerals in the controlled volume.:

$$\phi = 1 - \sum_{m=1}^{N_m} Y_{s,m} - Y_{s,inert} \quad (14)$$

Mineral dissolution or precipitation affects porosity, which influences permeability, fluid flow, and elastic properties. Empirical correlations between porosity changes and other petrophysical properties are used in the simulation. Users can specify additional mineralogy-specific correlations to model the interplay between geochemistry, geomechanics, and fluid flow in subsurface systems more accurately.

### 2.3.2. Matrix Permeability

Changes in porosity can also affect matrix permeability, which must be updated accordingly. The matrix permeability tensor  $k_m$  can be modified due to geochemical reactions through the application of the Carman-Kozeny equation (6, 14). Specifically, the matrix permeability tensor is calculated by Equation 15 where  $k_{m,ij}^0$  is the initial matrix permeability tensor, and  $\phi^0$  is the initial porosity, respectively.

$$k_{m,ij} = k_{m,ij}^0 \left( \frac{\phi}{\phi^0} \right)^3 \left( \frac{1 - \phi^0}{1 - \phi} \right)^2 \quad (15)$$

**Table 2:** Summary of the dispersion models implemented in porousMedia4Foam (36).

Name	Expression
None	$D_{iw} = 0$
Diffusion Only	$D_{iw} = D_{iw}^0 I$
Archie's Law	$D_{iw} = \phi^n D_{iw}^0 I$
Linear Dispersion	$D_{iw} = \phi^n \left\{ (D_{iw}^0 + \alpha_T  u_w ) I + \frac{(\alpha_L - \alpha_T)}{ u_w } u_w u_w \right\}$

### 2.3.3. Dispersion

Dispersion refers to the small-scale mechanical mixing and diffusion that occurs when one fluid displaces another miscibly (17). Although dispersion is often negligible in applications dominated by advection, MF3D-GC includes models for the effective diffusion and dispersion tensor  $D_{iw}$  built into the porousMedia4Foam module by Soulaire (36). Table 2 lists options for the effective diffusion and dispersion tensor  $D_{iw}$ . Here,  $D_{iw}^0$  denotes the molecular diffusion coefficient,  $\mathbf{I}$  is the unit tensor, and  $n$  is a user defined variable. Parameters  $\alpha_L$  and  $\alpha_T$  describe lateral and longitudinal dispersion, respectively.

A user can choose to ignore dispersion, consider only diffusion, or specify the dispersion tensor. The Archie's Law option includes tortuosity by introducing  $\phi^n$  into the model. The Linear Dispersion option includes diffusion, tortuosity, and dispersivity-velocity product. The model should be chosen carefully based on the application.

### 2.4. Kinetic Reaction Models

In MF3D-GC, users can specify the reaction models for mineral dissolution and precipitation as equilibrium or kinetic reactions. Suppose those are kinetics reaction, the kinetic reaction rate of mineral  $m$  (an element of the kinetic reaction  $R_k$ ), or  $r_m$ , is expressed as (Eq. 16) where  $A_s$  is the specific reactive surface area, and  $k_{km}$  is the apparent rate constant for mineral  $m$ .

$$r_m = A_{s,m} k_{km} \left(1 - \frac{Q_m}{K_m}\right) \quad (16)$$

$Q_m/K_m$  represents the saturation rate of mineral  $m$  with  $Q_m$  as the reaction quotient and  $K_m$  as the equilibrium dissolution constant. This term assumes dimensionless fitting parameters  $p$  and  $q$  equal to 1 (18, 28). The reaction rate depends on various physical properties, including surface area  $A_s$ , temperature  $T$ , and Gibbs energy (3).

Within the simulator, users can select the reactive surface area  $A_s$  and the apparent rate constant  $k_k$  from models in Sections 2.4.1 and 2.4.2. The code allows defining the kinetic reaction rate using the BASIC interpreter, originally embedded in PHREEQC and distributed with the Linux operating system (29, 49). Users can customize the reaction models and conditions for their specific study.

#### 2.4.1. Reactive Surface Area

Several methods for modeling the reactive surface area (or effective reactive surface area) are built in, as listed in Table 3 (36).

#### 2.4.2. Apparent Rate Constant

The apparent reaction rate constant  $k_k$  models the pH and temperature dependence of the reaction rate. In MF3D-GC, users can flexibly assign  $k_k$  according to the mineral description, as summarized in

Name	Expression
None	$A_s = 0$
Constant	$A_s = A_s^0$
Power-law	$A_s = A_s^0 (Y_{s,m})^n$
Sugar-lump	$A_s = \left[ A_s^0 + A_m \left\{ 1 - \left( \frac{Y_{s,m}}{Y_{s,m}^0} \right)^{n_1} \right\}^{n_2} \right] \left( \frac{Y_{s,m}}{Y_{s,m}^0} \right)^{n_3}$
Hydro-geochemical coupling	$A_s = A_s^0 \left( \frac{Y_{s,m}}{Y_{s,m}^0} \right)^n (1 - \exp(-Pe^{-p} Da^{-q}))$



**Table 4.** This table includes the forward rate reaction constant  $k_+$ , which refers to the dissolution reaction rate of minerals involving  $H^+$ ,  $H_2O$ , and  $OH^-$  (28). The formulation of  $k_+$  is (Eq. 17):

$$k_+ = k_{+,H} + k_{+,w} + k_{+,OH} \quad (17)$$

where  $k_{+,H}$ ,  $k_{+,w}$ , and  $k_{+,OH}$  denote the acid, neutral, and basic mechanisms for specific pH ranges (1.3-4.0, 5.6-8.2, and 8.6-10.3). Palandri and Kharaka (28) compiled these terms based on experimental rate data, available as a library script compatible with PHREEQC (49) (Table 4).

### 3. MODEL VALIDATION

This section validates the geochemical capabilities of MF3D-GC by comparing results with benchmarks from Xie et al. (46) and building on the validation work of the underlying porousMedia4Foam module (36). The benchmarks increase in geochemical and physical complexity, as shown in Table 5. Benchmark

**Table 5:** Overview of the benchmarks (46), showing the processes included in the benchmark by “○” marks in the table.

Level	1D/2D	Processes					$t_{end}$ [years]
		Advection	Dissolution	Precipitation	Redox	Diffusion	
B1	1D	○	○				150
B2	1D	○	○	○			150
B3	1D	○	○	○	○		300
B5	1D	○	○	○	○	○	300
B6	2D	○	○	○	○	○	300

1 (B1) is a simple 1D model with advective flow considering the calcite dissolution. Benchmark 2 (B2) adds gypsum precipitation to B1. Benchmark 3 (B3), Benchmark 5 (B5), and Benchmark 6 (B6) extend B2 with more complex chemical reactions, incorporating redox reactions and additional species. Benchmark 3 assumes advection-dominated flow without diffusion, while B5 and B6 include diffusion, with B6 expanding to 2D. Simulation results were compared for all benchmarks, focusing on B1 to B6. The original benchmark list included a diffusion dominated benchmark (B4), which is excluded here to focus on advection-dominated cases.

Benchmarks B1 to B5 assume a 1D model with flow over a 2-meter length, as illustrated in Figure 4. The cross-sectional area is 1 square meter to achieve consistency with the original benchmarks (46) and the

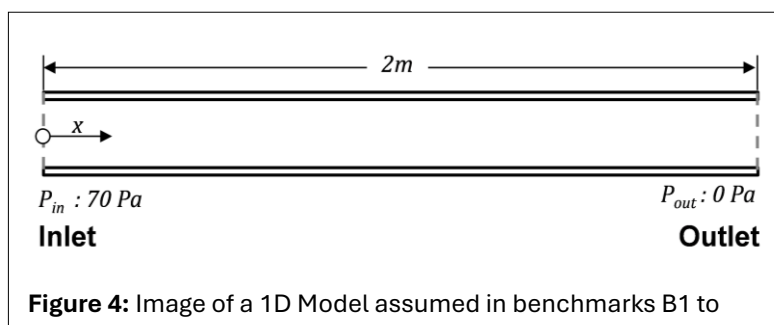


**Figure 4:** Image of a 1D Model assumed in benchmarks B1 to

validation by porousMedia4Foam (36). While Xie applied a hydraulic head difference of 0.007, Soulaire applied a fixed pressure of 70 Pa at the inlet and 0 Pa at the outlet, which this work follows. The 2-meter model for B1 to B5 is discretized into 80 cells (each 0.025 meter) with a time interval  $\Delta t$  of 21,600 seconds. The complexity of

**Table 6:** Initial and boundary conditions of the primary components for benchmark 1 (B1), calcite dissolution case.

Primary components	Units	Initial conditions	Boundary conditions
pH	-	9.38	3
Ca <sup>2+</sup>	mol/kg <sub>water</sub>	$1.56 \times 10^{-4}$	$9.97 \times 10^{-5}$
CO <sub>3</sub> <sup>2-</sup>	mol/kg <sub>water</sub>	$2.56 \times 10^{-4}$	$9.97 \times 10^{-3}$
SO <sub>4</sub> <sup>2-</sup>	mol/kg <sub>water</sub>	$9.97 \times 10^{-11}$	$6.44 \times 10^{-4}$

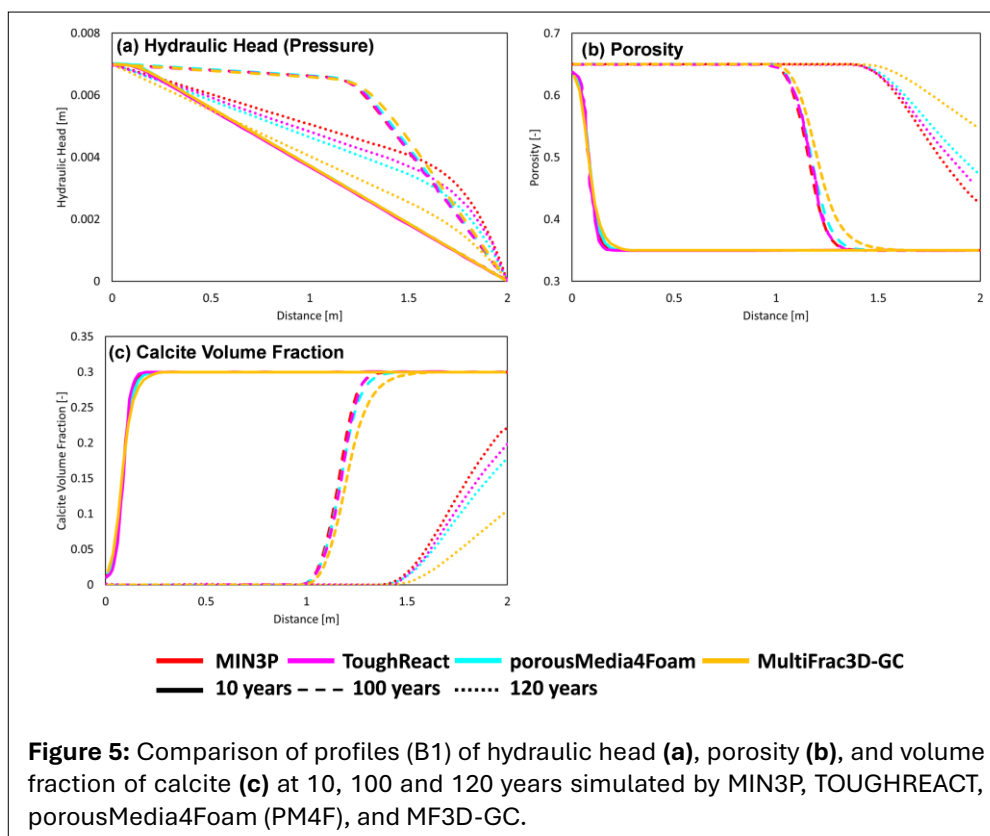
chemical reactions is based on fluid and mineral compositions detailed in Section 3.1 to 3.3. Section 3.4 describes a 2D model.

The discretization parameters were selected to align with previous works (36, 46). Both MIN3P and TOUGHREACT, referring Xie's work, implemented automatic timestep adjustment for unstable computations due to clogging or mineral phase disappearances (46). In contrast, this work and porousMedia4Foam maintained a fixed timestep of 21,600 seconds. PorousMedia4Foam divided timestep into six intervals for transport calculations, a method not used in MF3D-GC. These differences in numerical setting contribute to variation in results.

The benchmarks by Xie provide a comprehensive validation framework for testing MF3D-GC's geochemical capabilities. The following subsections detail the simulation setups and results for each benchmark, demonstrating that MF3D-GC can successfully simulate advection-dominated transport with varying geochemical complexities, including mineral dissolution, precipitation, and redox reactions. In addition, the model demonstrates both geochemical and geomechanical capabilities.

### 3.1. B1: Calcite Dissolution with Advective Transport

Benchmark 1 (B1) represents a simple 1D model where calcite dissolution alters flow properties in an advection-dominated flow. The model includes calcite and inert minerals with an initial volume fraction of 0.35 for pore space, 0.35 for inert mineral, and 0.30 for calcite. Initial porosity and permeability are 0.35 and  $1.186 \times 10^{-11} \text{ m}^2$ , varying with calcite dissolution. Table 6 lists the composition of in-place and



injected fluids. The pore space is initially saturated with an alkaline solution (pH 9.38) undersaturated with calcite. An acidic solution (pH 3) is injected to dissolve the calcite, treated as a kinetic reaction with a constant kinetic reaction rate of  $5 \times 10^{-5}$  mol/m<sup>2</sup>/s. The initial specific surface area is 1 m<sup>2</sup>/m<sup>3</sup> and decreases over time, following a power-law function with  $n$  of 2/3. The simulation is run for 150 years.

Simulation results for B1 were compared with reference models produced by MIN3P (21), TOUGHREACT (48), and porousMedia4FOAM (36). The comparison involved analyzing pressure, porosity, and calcite volume fraction at 10, 100, and 120 years, as illustrated in Figure 5. The results are color-coded: MIN3P in red, TOUGHREACT in magenta, porousMedia4FOAM in sky-blue, and MF3D-GC in orange. Line types indicate the time points: solid for 10 years, dashed for 100 years, and dotted for 120 years.

All simulated results show good agreement in pressure, porosity, and calcite volume fraction at 10 and 100 years. However, some variations appear at 120 years due to the dissolution front breakthrough, as previously noted by Xie et al (46). Overall, the comparison demonstrates that MF3D-GC effectively simulates calcite dissolution in advection-dominated flow, with results in good agreement with established models.

### 3.2. B2: Dissolution and Precipitation

Benchmark 2 adds complexity to B1 by including gypsum as a secondary mineral. The initial volume fractions are 0.35 for pore space, 0.35 for inert mineral, 0.30 for calcite, consistent with the setting of B1. Porosity, permeability, and specific surface area are the same as in B1. Calcite dissolution and gypsum precipitation are treated as kinetic reactions with constant kinetic reaction rates of  $5 \times 10^{-5}$  mol/m<sup>2</sup>/s and  $5 \times 10^{-5}$  mol/m<sup>2</sup>/s. The specific surface area of the primary mineral varies with porosity (power-law,  $n = 2/3$ ), while the specific surface area of secondary mineral is fixed. An acidic solution (pH 3.0) is introduced into the rock initially saturated with an alkaline solution (pH 9.33), as shown in Table 7. The in-place fluid is undersaturated with gypsum and in equilibrium with calcite, while the injected fluid is undersaturated with both minerals.

**Table 7:** Initial and boundary geochemical compositions in aqueous phase in benchmark 5 (B5).

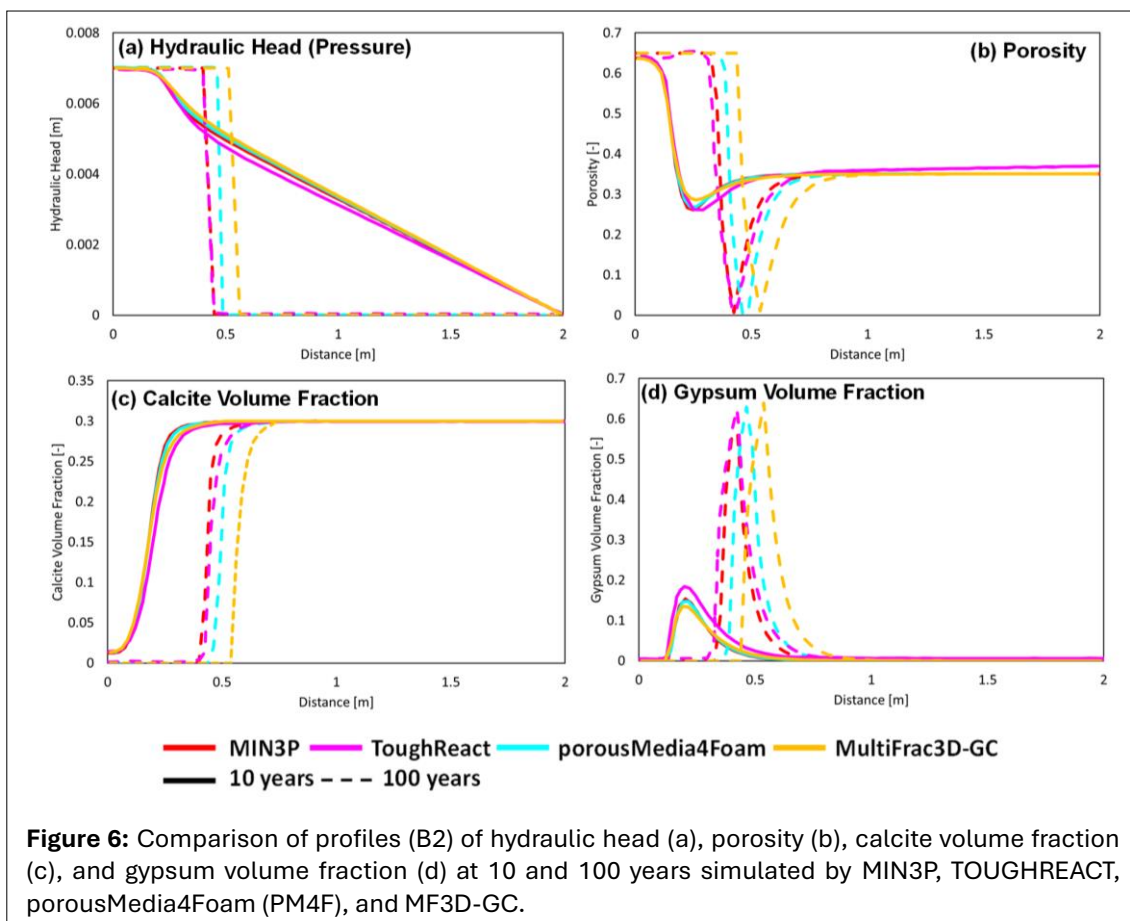
Primary components	Units	Initial conditions	Boundary conditions
pH	-	9.33	3.0
Ca <sup>2+</sup>	mol/kg <sub>water</sub>	$1.70 \times 10^{-4}$	$1.00 \times 10^{-4}$
CO <sub>3</sub> <sup>2-</sup>	mol/kg <sub>water</sub>	$2.70 \times 10^{-4}$	$1.00 \times 10^{-2}$
SO <sub>4</sub> <sup>2-</sup>	mol/kg <sub>water</sub>	$1.70 \times 10^{-4}$	0.2
Na <sup>+</sup>	mol/kg <sub>water</sub>	$3.20 \times 10^{-4}$	$3.96 \times 10^{-1}$

The simulated results for B2 are compared with the reference models, MIN3P, TOUGHREACT, and porousMedia4FOAM. Figure 6 illustrates pressure, porosity, calcite volume fraction, and gypsum volume fraction at 10 and 100 years. The color-code for the simulators match those in B1, with solid lines for 10 years and dashed lines for 100 years. In Figure 6a and b, pressure and porosity profiles show a sharp drop at 0.5 m from the inlet at 100 years due to gypsum precipitation. All models predict this drop in porosity where gypsum precipitates. Figure 6c and d show small discrepancies in the mineral volume fraction with overall good agreement among the simulators.

Benchmark 2 shows clogging at 0.5 meters from the inlet due to gypsum precipitation. The permeability, calculated using MultiFrac3D-GC, decreased from  $1.186 \times 10^{-16}$  m<sup>2</sup> to  $1.17 \times 10^{-19}$  m<sup>2</sup>, following the Carman-Kozeny equation. This reduction in injectivity led to slow the reaction propagation, resulting in minor differences between the 100 years and 120 years results. Consequently, the 120 years results are omitted from Figure 6 to maintain plot visibility.

### 3.3. B3: Redox Reaction

Benchmark 3 through B5 share identical fluid and mineral compositions, expanded from B2 to include more intricate chemical reaction, such as redox reactions, and additional species (Fe (II), Fe (III), K, Al, Na,



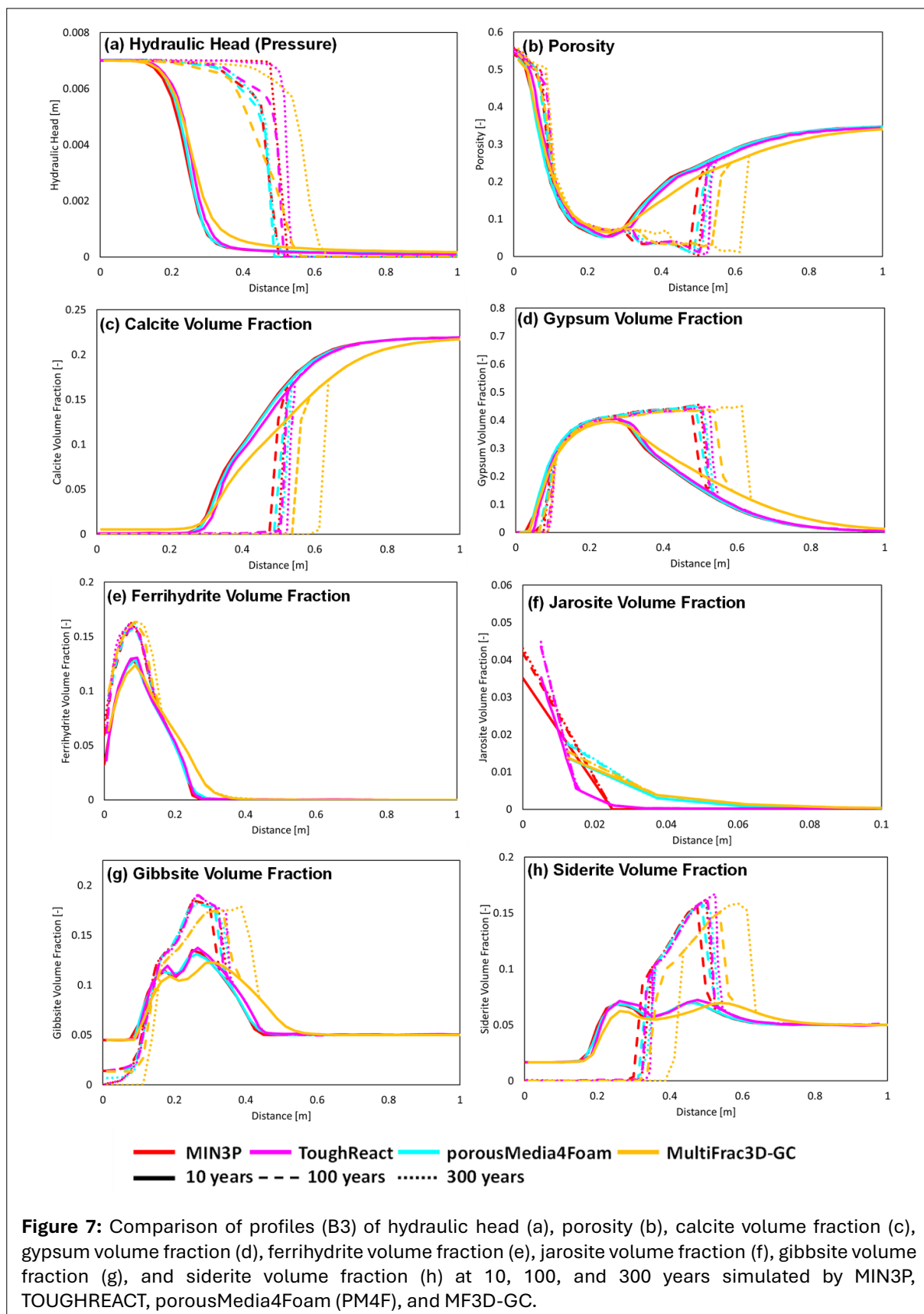
and O<sub>2</sub> (aq). Primary minerals are calcite, gibbsite, and siderite, while secondary minerals are gypsum, ferrihydrite, and jarosite. The initial homogeneous volume fractions are 0.35 for porosity, 0.35 for inert mineral, 0.22 for calcite, 0.05 for gibbsite, and 0.05 for siderite, as listed in Table 8. Initial porosity and permeability are 0.35 and  $1.186 \times 10^{-11} \text{ m}^2$ , varying with mineral dissolution and precipitation. All mineral dissolution and precipitation are treated as kinetic reactions with constant kinetic reaction rates listed in Table 9. The specific surface area of primary minerals varies with porosity (power-law,  $n = 2/3$ ), while the specific surface area of secondary minerals is fixed.

An acidic solution (pH 3.0) infiltrates the rock initially filled with an alkaline solution (pH 8.01). Metals cause redox reactions, as indicated in the in-place and injected fluid compositions in Table 9. Saturation index (SI) columns in Table 8 display the SI of minerals for initial conditions (IC) and boundary conditions (BC). Initially, the in-place fluid is undersaturated with gypsum and jarosite and in equilibrium with other minerals, while the injected fluid is oversaturated with jarosite but undersaturated with other minerals.

Benchmark 3 considers an advection-dominated flow scenario with dissolution, precipitation, and redox reactions and the associated alteration of flow properties. The simulation runs for 300 years. Results are

**Table 8:** Fractional volume, specific surface area, and saturation index of each mineral for benchmark 5 (B5). Saturation index corresponds to the in-place fluid at initial conditions (IC) and injected fluid as a boundary condition (BC) (46).

Mineral	Initial Volume Fraction	Kinetic reaction rate [mol/m <sup>2</sup> /s]	Saturation Index	
			I.C.	B.C.
Calcite	0.22	$5 \times 10^{-5}$	0.00	-8.93
Gypsum	0.00	$5 \times 10^{-5}$	-2.78	-2.02
Ferrihydrite	0.00	$5 \times 10^{-6}$	0.00	-0.07
Jarosite	0.00	$5 \times 10^{-6}$	-12.97	6.66
Gibbsite	0.05	$5 \times 10^{-7}$	0.00	-2.94
Siderite	0.05	$5 \times 10^{-6}$	0.00	-10.89



compared with reference models (MIN3P, TOUGHREACT, and porousMedia4FOAM). **Figure 7** illustrates pressure, porosity, and volume fractions of minerals at 10, 100, and 300 years. The color-codes match those in B with solid lines for 10 years, dashed for 100 years, and dotted for 300 years. The x-axis in **Figure 7** is scaled to focus on mineral dissolution and precipitation.

**Table 9:** Initial and boundary geochemical compositions in aqueous phase in benchmark 5 (B5).

Primary components	Units	Initial conditions	Boundary conditions
pH	-	8.01	3.0
pe	-	-0.67	17.53
Ca <sup>2+</sup>	mol/kg <sub>water</sub>	$4.71 \times 10^{-4}$	$1.00 \times 10^{-4}$
CO <sub>3</sub> <sup>2-</sup>	mol/kg <sub>water</sub>	$2.19 \times 10^{-3}$	$1.00 \times 10^{-2}$
SO <sub>4</sub> <sup>2-</sup>	mol/kg <sub>water</sub>	$1.70 \times 10^{-4}$	$1.00 \times 10^{-1}$
Na <sup>+</sup>	mol/kg <sub>water</sub>	$1.54 \times 10^{-3}$	$9.09 \times 10^{-2}$
Al <sup>3+</sup>	mol/kg <sub>water</sub>	$2.81 \times 10^{-7}$	$1.43 \times 10^{-2}$
K <sup>+</sup>	mol/kg <sub>water</sub>	$1.00 \times 10^{-5}$	$7.67 \times 10^{-5}$
Fe <sup>2+</sup>	mol/kg <sub>water</sub>	$6.59 \times 10^{-6}$	$1.14 \times 10^{-8}$
Fe <sup>3+</sup>	mol/kg <sub>water</sub>	$2.53 \times 10^{-8}$	$2.23 \times 10^{-2}$

While the general trends in mineral volume fractions computed using MF3D-GC align with other simulators, discrepancies are observed at 100 and 300 years, especially in pressure and volume fractions of calcite and gypsum. Xie et al (46) noted that minor porosity variations significantly impact fluid flow, affecting dissolution and precipitation propagation causing these discrepancies. Calcite and gypsum show relatively larger differences because of their higher kinetic reaction rates. Despite these challenges, MF3D-GC provides comparable results to other models in B3's complex geochemical setup.

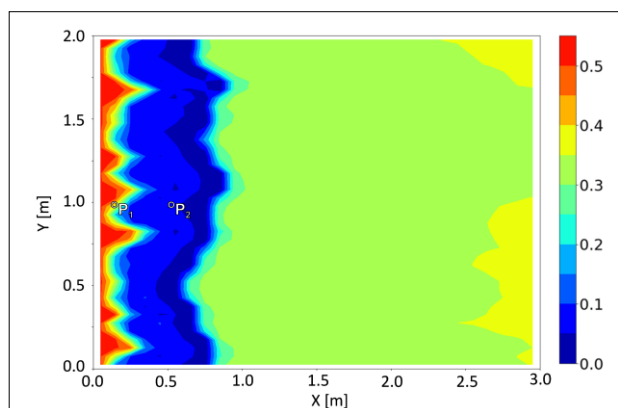


**Figure 8:** The porosity distribution after 300 years after starting acid injection. P1 and P2 are points chosen to display the porosity profile versus time in Figure 10b.

### 3.4. B6: 2-D Version of B6

Benchmark 6 extends B5 from a homogeneous 1D model to a heterogeneous 2D model, with the same fluid and mineral compositions as B3. The 2D model is 3 meters long and 2 meters high, as shown in Figure 8a, discretized into 1,200 cells (0.1m intervals in both directions). The porosity and specific surface area are the same as in B5, but permeability is heterogeneous, higher in the upper half than the lower half, as shown in Figure 8b. The flow is controlled by fixed pressure of 103 Pa at the inlet and 0 Pa at the outlet, maintaining the same pressure gradient as B1 to B5.

Benchmark 6 results demonstrate how permeability heterogeneity affects property distribution. Figure 9 displays porosity at 300

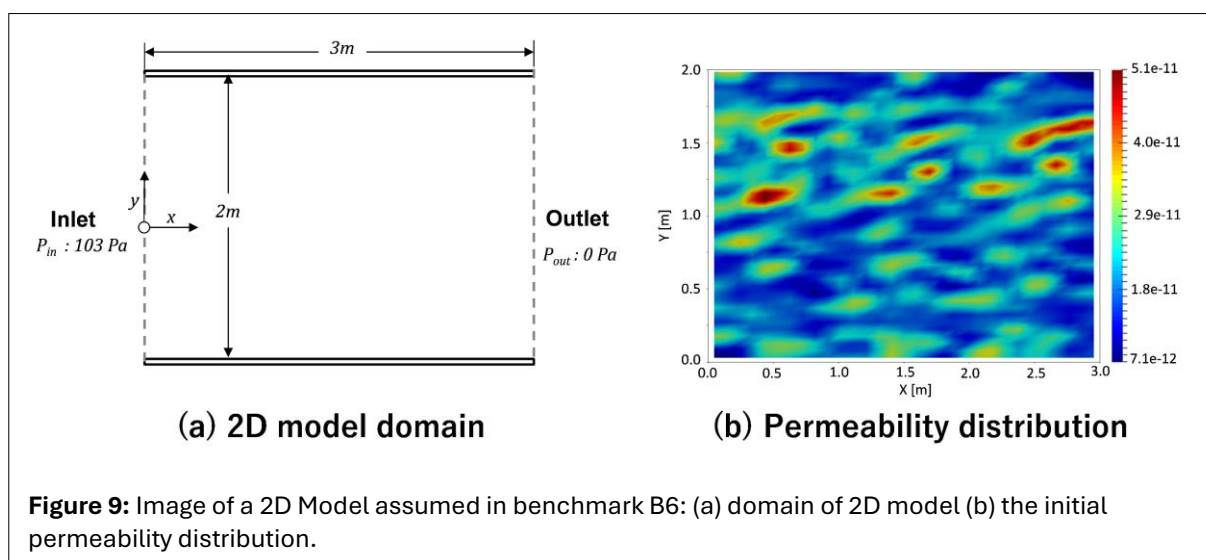
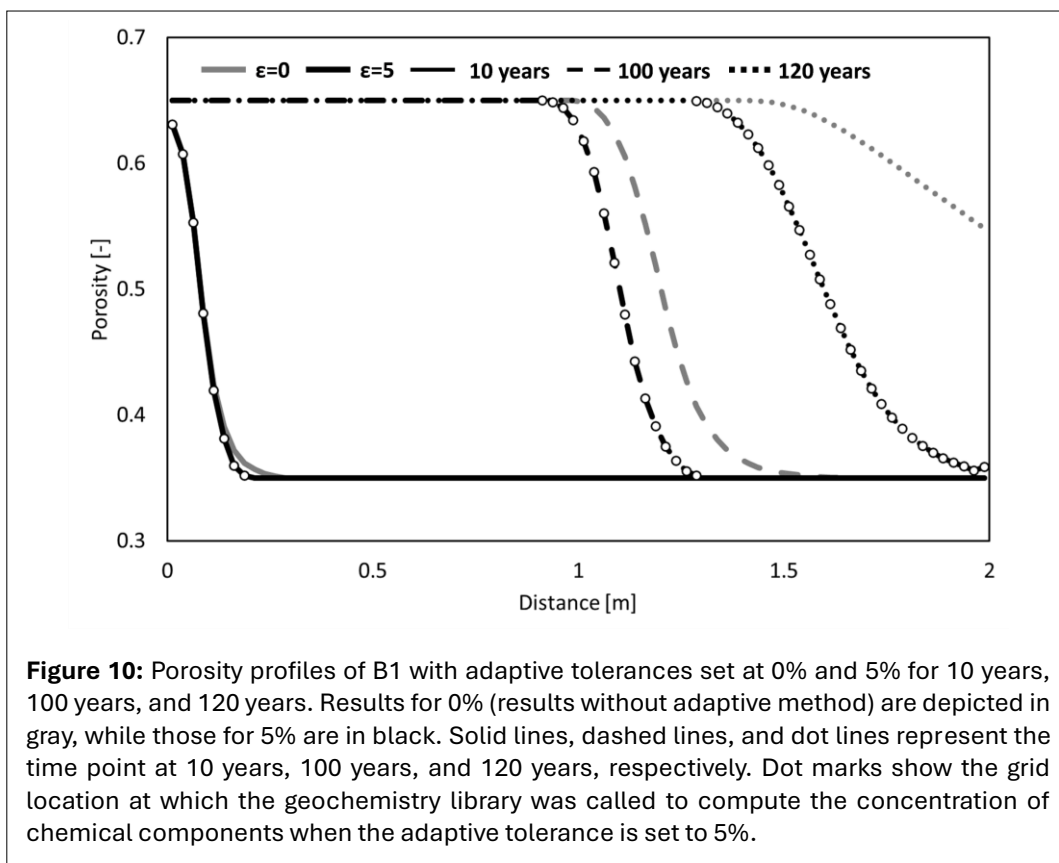
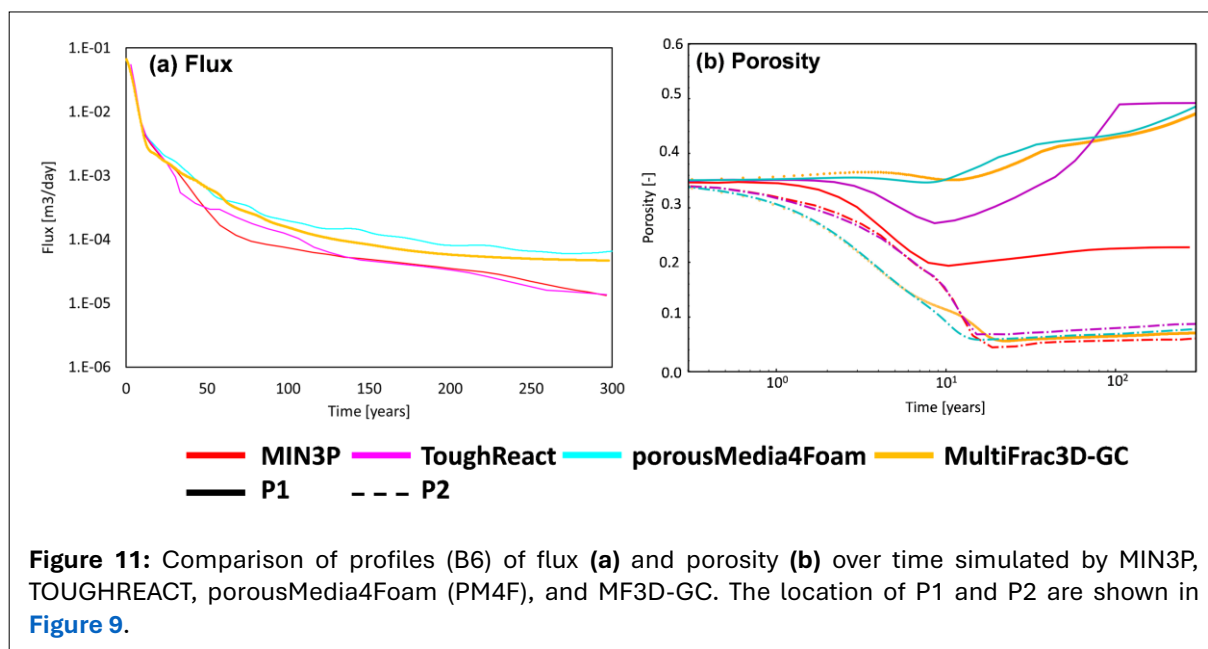


**Figure 9:** Image of a 2D Model assumed in benchmark B6: (a) domain of 2D model (b) the initial permeability distribution.



years after starting acid injection, highlighting selective flow due to heterogeneous permeability, resulting in significant spatial variations in mineral-fluid chemical reactions. High porosity zones appear in red, moderate in yellow to green, and low in blue. This trend is like B5, but propagation varies in the y-direction due to permeability heterogeneity.

Despite local flow differences, the global trend aligns well with other simulators (MIN3P, TOUGHREACT, and porousMedia4FOAM), as shown in **Figure 10a**. The computed flux at the outlet gradually decreases over time. The porosity comparison also shows good agreement as shown in **Figure 10b**, displaying porosity evolution at two locations, P1 and P2. As illustrated in **Figure 11**, P1 is in a high porosity zone, and P2 is in a low porosity zone at 300 years. All simulators show increasing porosity at P1 and decreasing at P2. Therefore, the results are comparable in the 2D case with complex physical and geochemical settings.



## 4. ILLUSTRATION OF GEOCHEMISTRY CAPABILITIES IN MF3D-GC

This section discusses two new features incorporated into the MF3D-GC model beyond the original capabilities of porousMedia4Foam. [Section 4.1](#) explores using an adaptive tolerance approach to reducing computing time, while [Section 4.2](#) examines the effect of making the apparent kinetic reaction rate a function of temperature and pH. The cases are based on B1, an advection-dominated case with calcite dissolution. As shown in [Table 10](#), the original B1 used no adaptive tolerance and a constant kinetic reaction rate. In [Section 4.1](#), adaptive tolerance ranges from 0% to 10% to study its impact on computing time and accuracy (B1 (a)). In [Section 4.2](#), two kinetic reaction rates are compared: a constant kinetic reaction rate (B1(b.1)) and a kinetics reaction rate as a function of temperature and pH (B1(b.2)). These results guide using the MF3D-GC model with these new features.

### 4.1. Performance Evaluation of Adaptive Tolerance Approach

**Table 10:** Overview of cases used to evaluate the Adaptive Tolerance feature in MF3D-GC.

Level	1D/2D	Processes				$t_{end}$ [years]
		Advection	Dissolution	Adaptive tolerance	Kinetics Setting	
B1	1D	○	○	0%	Constant value	200
B1(a)	1D	○	○	0~10%	Constant value	200
B1(b.1)	1D	○	○	5%	Constant value	200
B1(b.2)	1D	○	○	5%	Function of pH and T	200

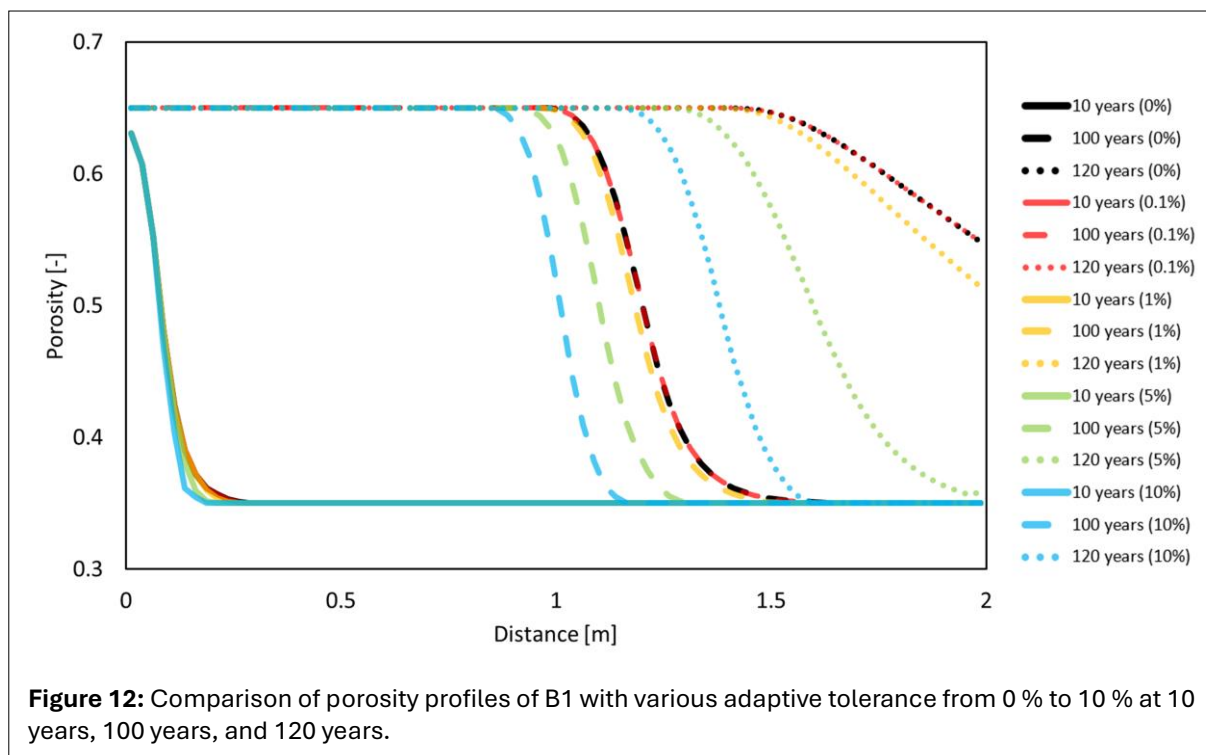
This section investigates the performance of the adaptive tolerance approach ([Section 2.2.2](#)) by comparing simulation results with adaptive tolerances range from 0 % to 10 %. The case settings are based on B1 ([Section 3.1](#)) with an adaptive tolerance of 0%.

The adaptive tolerance approach reduces the calculations needed for geochemical reactions, which are time-consuming in reactive-transport simulators. [Figure 11](#) illustrates the porosity profile with adaptive tolerances of 0% and 5% at 10, 100, and 120 years. Results for 0% adaptive tolerance, equivalent to the original results without the adaptive method, are represented in gray, while those for 5% are depicted in black. Porosity values with dot marks, considering both transport and chemical reactions, appear only along reaction fronts. In this case, using a recommended adaptive tolerance of 5% halved the computing with minimal accuracy loss at 10 and 100 years.

The relationship between adaptive tolerance magnitude and accuracy is investigated in [Figure 12](#), which shows porosity profiles with various adaptive tolerance at 10, 100, and 120 years. The 0% adaptive tolerance results (the original results) are displayed in black lines, while other results range from hot to cool colors with increasing adaptive tolerance (0.1 % to 10 %). The 0.1% tolerance matches the original results perfectly at all time points, reducing computation time to 60%. Other results show good agreement at 10 years (solid lines), but discrepancies from the original result increase over time for higher adaptive tolerance. Higher adaptive tolerances underestimate the calcite dissolution, causing errors and delays in reaction propagation at 100 and 120 years.

The adaptive method improves computing efficiency while maintaining high accuracy. However, selecting the appropriate adaptive tolerance value is crucial based on the simulation's objective. Overall, the adaptive tolerance approach is valuable for enhancing efficiency in long-duration simulations with complex geochemical reactions.





## 4.2. Comparison of Kinetic Reaction Rate Models

MF3D-GC allows user-defined kinetic reaction models via BASIC scripts. Benchmarks in Section 3 assumed a constant reaction rate for minerals. This section compares B1 using two different apparent kinetic reaction rates models: a constant value of  $5 \times 10^{-5}$  mol/m<sup>2</sup>/s (Case 1) and a rate dependent on temperature and pH (Case 2). An adaptive tolerance of 5% is used in both cases to reduce computing time.

The components of the apparent kinetic reaction rate constant  $k_k$  for calcite ( $k_{+,H}$ ,  $k_{+,w}$ , and  $k_{+,OH}$ ), as a function of temperature and pH, are given as shown below (Eq. 18) in the database, where  $R$  is the gas constant,  $T$  is the temperature, and  $\alpha_{HCO_3^-}$  is the activity of  $HCO_3^-$  (28).

$$0, 6.59 \times 10^4 e^{-66000/RT}, 1.04 \times 10^9 e^{-67000/RT} \alpha_{HCO_3^-}^{1.6} \quad (18)$$

In this isothermal case, the temperature remains constant at 25°C, so the calcite dissolution rate varies only with pH. The rate function is introduced into the code using BASIC scripts (49).

Figure 13 compares Case 1 (black lines) and Case 2 (gray lines) at 10, 100, and 120 years. Ignoring pH effects underestimate chemical concentration at low pH and overestimates them at high pH. Differences accumulate over time due to varying mineral properties. While more complex models improve accuracy, they also increase computing time. Users should carefully select minerals and property models to balance accuracy and computing efficiency for evaluating geochemical reactions in long-term CO<sub>2</sub> sequestration.

## 4.3. Coupling Geochemistry with Geomechanics and Flow

This section demonstrates geochemistry and geomechanics coupling capabilities using two cases: one based on benchmarks in previous sections (Section 4.3.1), and the other from our previous work (Section 4.3.2).

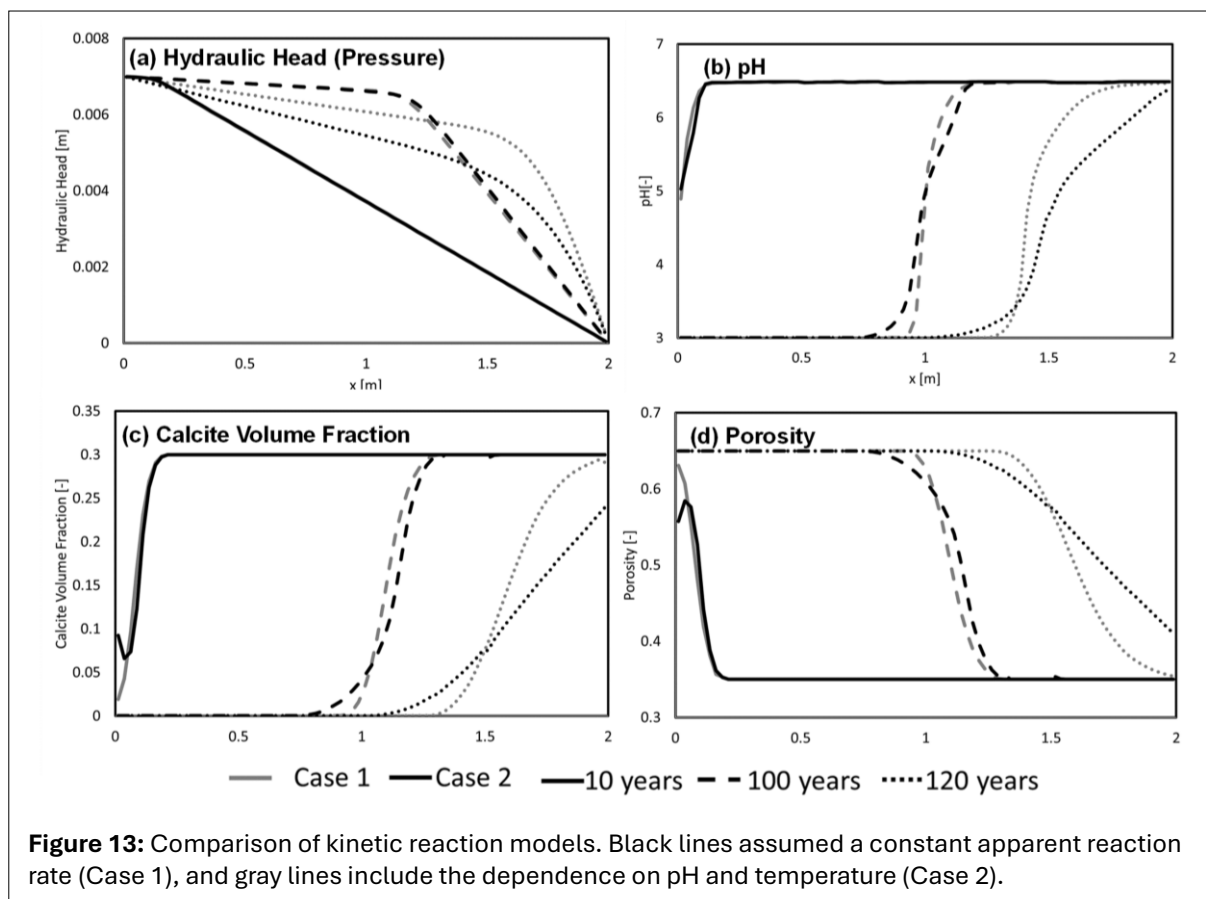


**Figure 13:** Comparison of kinetic reaction models. Black lines assumed a constant apparent reaction rate (Case 1), and gray lines include the dependence on pH and temperature (Case 2).

#### 4.3.1. Benchmark Results

Stress and deformation profiles are shown for a 2D domain from B6 with geochemical settings from B2. The geomechanical settings allow to move freely with zero constraining stress, and the Biot coefficient is set to 1.0. **Figure 14** illustrates the results after 10 years of acid flow into the 2D model with calcite and inert minerals. Similar to B2, porosity increases near the inlet due to calcite dissolution and decreases around  $x = 0.5$  m due to gypsum precipitation (**Figure 14a**). The heterogeneous permeability distribution (**Figure 8b**) causes non-uniform porosity in  $z$ -direction, affecting pressure and stress propagation (**Figure 8b** and **c**). Stress is linked to displacement (**Figure 14d**), with higher displacement along the inlet due to elevated total stress corresponding to high pore pressure. The high displacement region, colored red, is larger in the upper half due to permeability heterogeneity. The stress distribution from lateral and vertical heterogeneity in pressure and permeability leads to a small displacement zone at the bottom left. These results demonstrate the impact of mineral dissolution and precipitation on geomechanical properties.

#### 4.3.2. Previous Work on Fractured Sandstones Case Study

This example uses a study on  $\text{CO}_2$ -rich water injection into fractured sandstones and carbonates to showcase the simulator's geomechanics capabilities (22).

**Figure 15** illustrates the geochemical interactions between  $\text{CO}_2$ -rich brine and reservoir minerals in sandstone, with quartz as the reactive component. The model geometry with the injector at the center and a planer fracture is shown in part **a**, porosity in part **b**, deformation in part **c**, and effective stress in part **d** after short period of  $\text{CO}_2$ -rich brine injection. Significant changes in porosity and permeability were observed due to mineral dissolution and precipitation along the fracture, impacting the mechanical and flow properties of the reservoir rocks (**Figure 15b**).

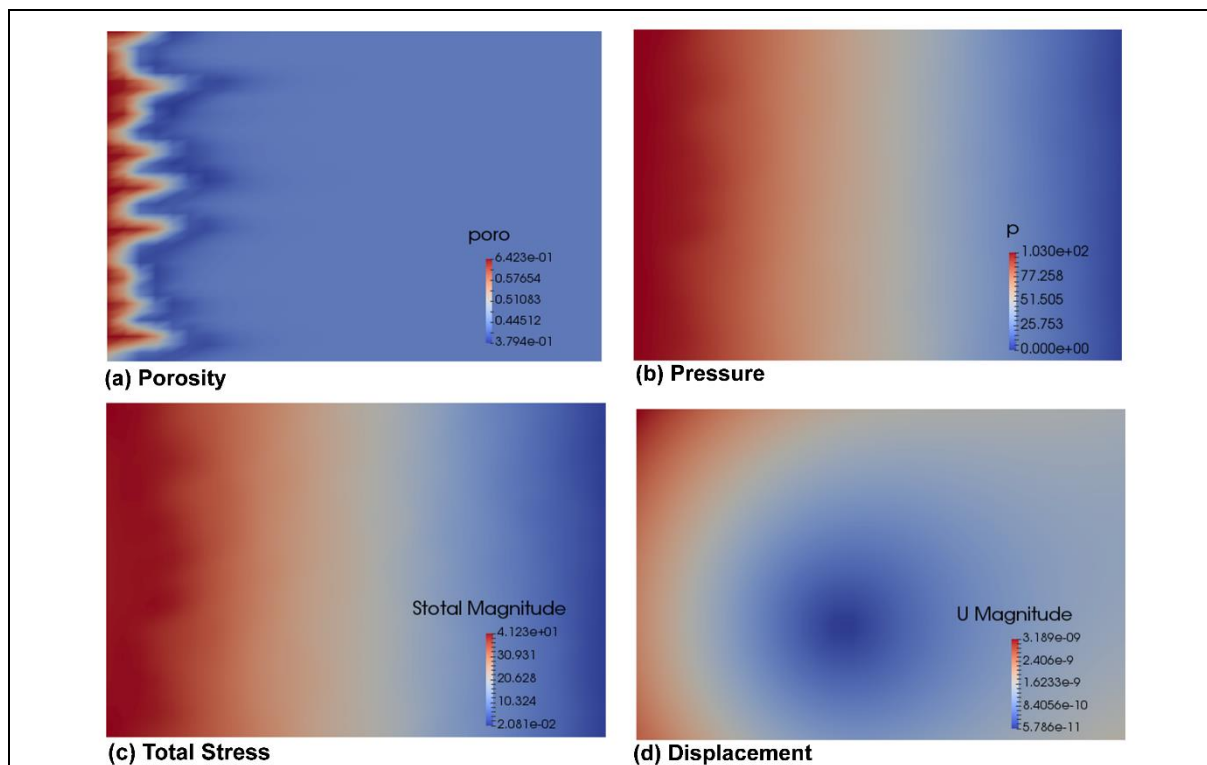


**Figure 14:** Distribution of hydraulic and geomechanical properties after 10 years of flow: **(a)** porosity, **(b)** pressure, **(c)** total stress, and **(d)** displacement.

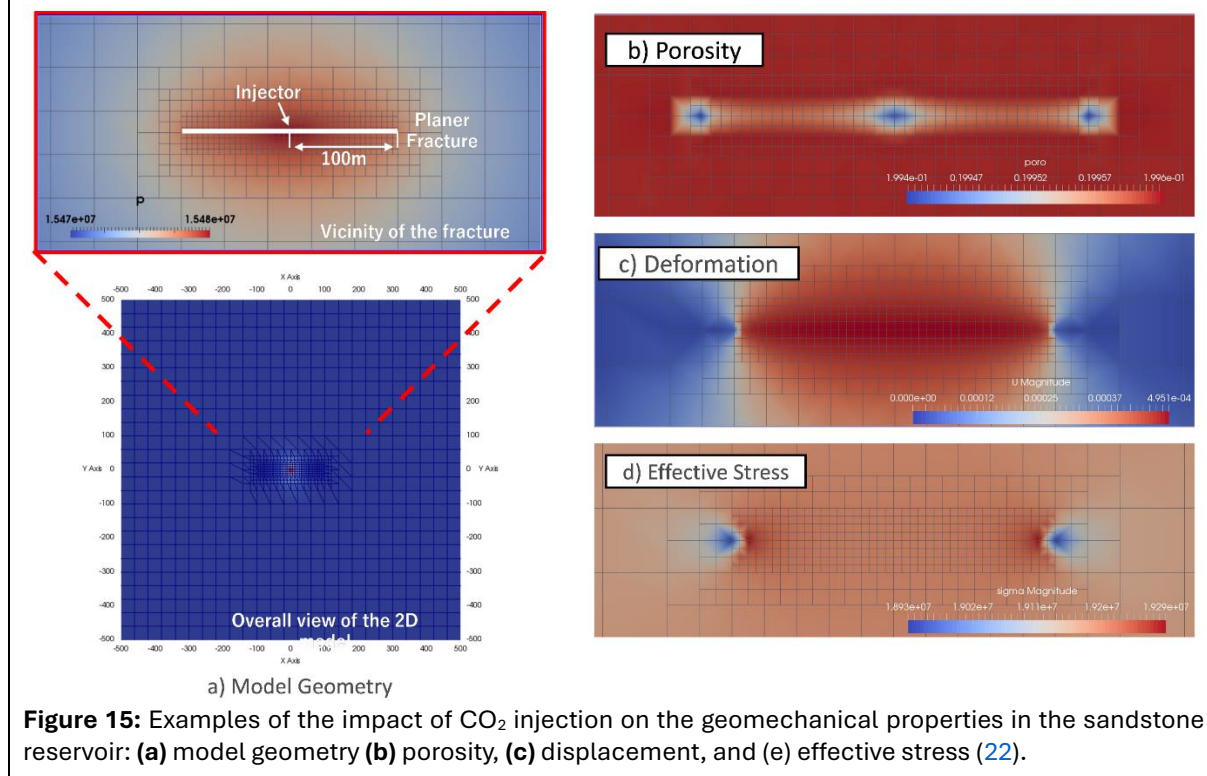


**Figure 15:** Examples of the impact of CO<sub>2</sub> injection on the geomechanical properties in the sandstone reservoir: **(a)** model geometry **(b)** porosity, **(c)** displacement, and **(e)** effective stress (22).

The geomechanics coupling revealed dynamic stress and deformation evolution (**Figure 15c** and **d**). Decreased porosity led to localized zones of higher stress and displacement, particularly near the fracture tips and injector where CO<sub>2</sub>-rich brine interacted more intensively with the minerals. The simulation results demonstrated that fracture geometry and mineral composition significantly influenced the extent and location of stress changes and deformation. The combined effects of chemical reactions and

geomechanical changes indicated a potential increased fracture growth and propagation. These results highlight the importance of integrating geochemical reactions with geomechanical simulations to accurately predict subsurface system behavior under CO<sub>2</sub> injection conditions. The findings demonstrate the importance of considering both geomechanical and geochemical processes in assessing the long-term stability and effectiveness of CO<sub>2</sub> sequestration projects.

## 5. CONCLUSION

This study presents MF3D-GC, a new 3D geochemical model that couples fluid flow and geomechanics by incorporating PhreeqcRM into MF3D. MF3D-GC's capabilities as a reactive-transport simulator are validated through benchmark comparisons, showing good agreement with other reactive-transport simulators. It allows user-defined kinetic models dependent on specific surface area, saturation state, temperature, and pH, enhancing accuracy but reducing computational efficiency. Selecting minerals and models requires balancing accuracy and computational efficiency.

To address the high computational cost of reactive transport simulation, an adaptive tolerance method was implemented. This method effectively reduces computation time, but the choice of adaptive tolerance parameters should be made carefully to maintain accuracy.

This work also demonstrated the coupling between geochemistry and geomechanics, extending beyond conventional reactive transport simulators. Results highlighted that mineral precipitation and dissolution affect stress and displacement through pressure changes. Enhancing the model's coupling of geochemistry and geomechanics requires considering the alterations in geomechanical properties induced by geochemistry.

The results presented in this work successfully validate the MF3D-GC, a versatile, 3D, single-phase reactive transport model. The code can be applied to solution mining, geothermal energy production, and CO<sub>2</sub> sequestration.

---

### **KEY POINTS:**

*We developed a new 3D model that couples subsurface geochemistry with fluid flow and geomechanics.*

*The model was validated through comparisons with other reactive-transport simulators for several benchmarked cases.*

*An adaptive tolerance method was implemented to address the high computational cost of reactive transport simulation.*

---

## STATEMENTS AND DECLARATIONS

### Supplementary Material

An Appendix is available online for downloading [here](#).

### Acknowledgements

The authors wish to acknowledge the financial support provided by the Joint Industry Project on Hydraulic Fracturing and Sand Control at the University of Texas at Austin.

### Author Contributions

Miki Mura: Conceptualization, Data Curation, Formal Analysis, Investigation, Methodology, Project Administration, Software, Validation, Visualization, Writing – Original Draft, Writing – Review & Editing.

Shuang Zheng: Software, Writing – Review & Editing.

Mukul M. Sharma: Conceptualization, Funding Acquisition, Methodology, Project Administration, Resources, Supervision, Writing – Review & Editing.

## Conflicts of Interest



To the best of our knowledge there are no conflicts of interest for any of the authors.

## Data, Code & Protocol Availability

The code discussed in this paper, pertaining to the integration of geochemistry within an existing geomechanics-flow framework (MF3D), was collaboratively developed by our research group. Due to the collaborative nature of the codebase and considerations surrounding intellectual property rights and collaborative agreements, we are unable to provide open access to the code.

For inquiries regarding the code or further questions, please contact the author Miki Mura ([miki.mura@autin.utexas.edu](mailto:miki.mura@autin.utexas.edu)). We appreciate your understanding and remain committed to transparency within the constraints of our collaborative agreements.

## ORCID IDs

Miki Mura  <https://orcid.org/0000-0003-0610-0099>  
 Shuang Zheng  <https://orcid.org/0000-0002-7816-1176>  
 Mukul Sharma  <https://orcid.org/0009-0005-5369-790X>

## REFERENCES

1. Abd, A. S., & Abushaikh, A. (2019). A review of numerical modelling techniques for reactive transport in subsurface reservoirs and application in mimetic finite difference discretization schemes. SPE Europec Featured at 81st EAGE Conference and Exhibition, D021S001R012. <https://doi.org/10.2118/195558-MS>
2. Bissell, R. C., Vasco, D. W., Atbi, M., Hamdani, M., Okwelegbe, M., & Goldwater, M. H. (2011). A full field simulation of the in Salah gas production and CO<sub>2</sub> storage project using a coupled geo-mechanical and thermal fluid flow simulator. *Energy Procedia*, 4, 3290–3297. <https://doi.org/10.1016/j.egypro.2011.02.249>
3. Black, J. R., Carroll, S. A., & Haese, R. R. (2015). Rates of mineral dissolution under CO<sub>2</sub> storage conditions. *Chemical Geology*, 399, 134–144. <https://doi.org/10.1016/j.chemgeo.2014.09.020>
4. Bordeaux-Rego, F., Sanaei, A., & Sepehrnoori, K. (2022). Enhancement of simulation CPU time of reactive-transport flow in porous media: Adaptive tolerance and mixing zone-based approach. *Transport in Porous Media*, 143(1), 127–150. <https://doi.org/10.1007/s11242-022-01789-1>
5. Cardiff, P., Tuković, Ž., Jasak, H., & Ivanković, A. (2016). A block-coupled Finite Volume methodology for linear elasticity and unstructured meshes. *Computers & Structures*, 175, 100–122. <https://doi.org/10.1016/j.compstruc.2016.07.004>
6. Carman, P. C. (1997). Fluid flow through granular beds. *Chemical Engineering Research and Design*, 75, S32–S48. [https://doi.org/10.1016/S0263-8762\(97\)80003-2](https://doi.org/10.1016/S0263-8762(97)80003-2)
7. Computer Modelling Group Ltd. (2019). CMG Licensing User Guide no. 2. Guide to Using CMG Licensing.
8. Gai, X. (2004). A coupled geomechanics and reservoir flow model on parallel computers [Ph.D. Dissertation, The University of Texas at Austin]. <https://repositories.lib.utexas.edu/handle/2152/1187>
9. Goerke, U.-J., Park, C.-H., Wang, W., Singh, A. K., & Kolditz, O. (2011). Numerical simulation of multiphase hydromechanical processes induced by CO<sub>2</sub> injection into deep saline aquifers. *Oil & Gas Science and Technology – Revue d'IFP Energies Nouvelles*, 66(1), 105–118. <https://doi.org/10.2516/ogst/2010032>
10. Goertz-Allmann, B. P., Kühn, D., Oye, V., Bohloli, B., & Aker, E. (2014). Combining microseismic and geomechanical observations to interpret storage integrity at the In Salah CCS site. *Geophysical Journal International*, 198(1), 447–461. <https://doi.org/10.1093/gji/ggu010>
11. Jaeger, J. C., Cook, N. G. W., & Zimmerman, R. W. (2007). Fundamentals of rock mechanics (4th ed). Blackwell Pub.
12. Jasak, H., & Weller, H. G. (2000). Application of the finite volume method and unstructured meshes to linear elasticity. *International Journal for Numerical Methods in Engineering*, 48(2), 267–287. [https://doi.org/10.1002/\(SICI\)1097-0207\(20000520\)48:2<267::AID-NME884>3.0.CO;2-Q](https://doi.org/10.1002/(SICI)1097-0207(20000520)48:2<267::AID-NME884>3.0.CO;2-Q)
13. Kazemi Nia Korrani, A., Sepehrnoori, K., & Delshad, M. (2015). Coupling IPHreeqc with UTCHEM to model reactive flow and transport. *Computers & Geosciences*, 82, 152–169. <https://doi.org/10.1016/j.cageo.2015.06.004>

14. Kozeny, J. (1927). Ueber kapillare Leitung des Wassers im Boden [About capillary conduction of water in the soil]. *Sitzungsber Akad., Wiss., Wien*, 136(2a), 271–306.
15. Kvamme, B., & Liu, S. (2009). Reactive transport of CO<sub>2</sub> in saline aquifers with implicit geomechanical analysis. *Energy Procedia*, 1(1), 3267–3274. <https://doi.org/10.1016/J.EGYPRO.2009.02.112>
16. Lake, L. W., Bryant, S. L., & Araque-Martinez, A. N. (2002). *Geochemistry and fluid flow*. In: *Geochemistry and fluid flow* (1st ed.). Elsevier Science Ltd.
17. Lake, L. W., Johns, Russell, & Rossen, Bill. (2014). *Fundamentals of Enhanced Oil Recovery*. (1st ed.). SPE.
18. Lasaga, A. C. (2018). Chapter 2. Fundamental approaches in describing mineral dissolution and precipitation rates. In A. F. White & S. L. Brantley (Eds.), *Chemical Weathering Rates of Silicate Minerals* (pp. 23–86). De Gruyter. <https://www.degruyter.com/document/doi/10.1515/9781501509650-004/html>
19. Lucier, A., Zoback, M., Gupta, N., & Ramakrishnan, T. S. (2006). Geomechanical aspects of CO<sub>2</sub> sequestration in a deep saline reservoir in the Ohio River Valley region. *Environmental Geosciences*, 13(2), 85–103. <https://doi.org/10.1306/eg.11230505010>
20. Manchanda, R. (2016). A general poro-elastic model for pad-scale fracturing of horizontal wells. University of Texas at Austin [Dissertation]. <https://doi.org/10.15781/T2DD66>
21. Mayer, K. U., Frind, E. O., & Blowes, D. W. (2002). Multicomponent reactive transport modeling in variably saturated porous media using a generalized formulation for kinetically controlled reactions. *Water Resources Research*, 38(9). <https://doi.org/10.1029/2001WR000862>
22. Mura, M., & Sharma, M. M. (2023). Flow-geomechanics-geochemistry simulation of CO<sub>2</sub> injection into fractured sandstones and carbonates. Day 2 Tue, October 17, 2023, D021S020R001. <https://doi.org/10.2118/215032-MS>
23. Oelkers, E. H., Gislason, S. R., & Matter, J. (2008). Mineral carbonation of CO<sub>2</sub>. *Elements*, 4(5), 333–337. <https://doi.org/10.2113/gselements.4.5.333>
24. Oliveira, T. D. S., Blunt, M. J., & Bijeljic, B. (2019). Modelling of multispecies reactive transport on pore-space images. *Advances in Water Resources*, 127, 192–208. <https://doi.org/10.1016/j.advwatres.2019.03.012>
25. Olivella, S., Carrera, J., Gens, A., & Alonso, E. E. (1994). Nonisothermal multiphase flow of brine and gas through saline media. *Transport in Porous Media*, 15(3), 271–293. <https://doi.org/10.1007/BF00613282>
26. Onaisi, Atef, Samier, Pierre, Koutsabeloulis, Nick, and Pascal Longuemare. "Management of Stress Sensitive Reservoirs Using Two Coupled Stress-Reservoir Simulation Tools: ECL2VIS and ATH2VIS." Paper presented at the Abu Dhabi International Petroleum Exhibition and Conference, Abu Dhabi, United Arab Emirates, October 2002. <https://doi.org/10.2118/78512-MS>
27. Orlic, B. (2009). Some geomechanical aspects of geological CO<sub>2</sub> sequestration. *KSCCE Journal of Civil Engineering*, 13(4), 225–232. <https://doi.org/10.1007/s12205-009-0225-2>
28. Palandri, J. L., Kharaka, Y. K., & Survey, U. S. G. (2004). A compilation of rate parameters of water-mineral interaction kinetics for application to geochemical modeling. In Open-File Report. <https://doi.org/10.3133/ofr20041068>
29. Parkhurst, D. L., Appelo, C. A. J. (2013). Description of input and examples for PHREEQC version 3: a computer program for speciation, batch-reaction, one-dimensional transport, and inverse geochemical calculations. Chapter 42 of Section A: Groundwater In: Book 6 Modeling Techniques. <https://doi.org/10.3133/tm6A43>
30. Parkhurst, D. L., & Wissmeier, L. (2015). PhreeqcRM: A reaction module for transport simulators based on the geochemical model PHREEQC. *Advances in Water Resources*, 83, 176–189. <https://doi.org/10.1016/j.advwatres.2015.06.001>
31. Rutqvist, J. (2011). Status of the TOUGH-FLAC simulator and recent applications related to coupled fluid flow and crustal deformations. *Computers & Geosciences*, 37(6), 739–750. <https://doi.org/10.1016/j.cageo.2010.08.006>
32. Rutqvist, J. (2012). The geomechanics of CO<sub>2</sub> storage in deep sedimentary formations. *Geotechnical and Geological Engineering*, 30(3), 525–551. <https://doi.org/10.1007/s10706-011-9491-0>
33. Rutqvist, J., & Tsang, C.-F. (2002). A study of caprock hydromechanical changes associated with CO<sub>2</sub>-injection into a brine formation. *Environmental Geology*, 42(2–3), 296–305. <https://doi.org/10.1007/s00254-001-0499-2>
34. Sanaei, A. (2019). Compositional Reactive-Transport Modeling of Engineered Waterflooding. University of Texas at Austin [Dissertation]. <http://dx.doi.org/10.26153/tsw/13775>
35. Sevougian, S. D., Schechter, R. S., & Lake, L. W. (1993). Effect of Partial Local Equilibrium on the Propagation of Precipitation/Dissolution Waves. *Industrial & Engineering Chemistry Research*, 32(10), 2281–2304. <https://doi.org/10.1021/ie00022a013>
36. Soulaire, C., Pavuluri, S., Claret, F., & Tournassat, C. (2021). Porousmedia4foam: Multi-scale open-source platform for hydro-geochemical simulations with OpenFOAM®. *Environmental Modelling & Software*, 145, 105199. <https://doi.org/10.1016/j.envsoft.2021.105199>

37. Steefel, C. I., Appelo, C. A. J., Arora, B., Jacques, D., Kalbacher, T., et al. (2015). Reactive transport codes for subsurface environmental simulation. *Computational Geosciences*, 19(3), 445–478. <https://doi.org/10.1007/s10596-014-9443-x>
38. Steefel, C. I., & MacQuarrie, K. T. B. (1996). Chapter 2. Approaches to modeling of reactive transport in porous media. In P. C. Lichtner, C. I. Steefel, & E. H. Oelkers (Eds.), *Reactive Transport in Porous Media* (pp. 83–130). De Gruyter. <https://doi.org/10.1515/9781501509797-005>
39. Tang, T. (2013). Implementation of solid body stress analysis in OpenFOAM. [https://backend.orbit.dtu.dk/ws/portalfiles/portal/53911239/prod11365072351121.OSCFD\\_Report\\_TianTang\\_peerReviewed.pdf](https://backend.orbit.dtu.dk/ws/portalfiles/portal/53911239/prod11365072351121.OSCFD_Report_TianTang_peerReviewed.pdf)
40. Tang, T., Hededal, O., & Cardiff, P. (2015). On finite volume method implementation of poro-elasto-plasticity soil model. *International Journal for Numerical and Analytical Methods in Geomechanics*, 39(13), 1410–1430. <https://doi.org/10.1002/NAG.2361>
41. Taron, J., Elsworth, D., & Min, K.-B. (2009). Numerical simulation of thermal-hydrologic-mechanical-chemical processes in deformable, fractured porous media. *International Journal of Rock Mechanics and Mining Sciences*, 46(5), 842–854. <https://doi.org/10.1016/j.ijrmms.2009.01.008>
42. Tian, H., Xu, T., Li, Y., Yang, Z., & Wang, F. (2015). Evolution of sealing efficiency for CO<sub>2</sub> geological storage due to mineral alteration within a hydrogeologically heterogeneous caprock. *Applied Geochemistry*, 63, 380–397. <https://doi.org/10.1016/j.apgeochem.2015.10.002>
43. UT Austin. (2000). Volume I: User's Guide for UTCHEM-9.0. A Three-Dimensional Chemical Flood Simulator. [http://gmsdocs.aquaveo.com/UTCHEM\\_Users\\_Guide.pdf](http://gmsdocs.aquaveo.com/UTCHEM_Users_Guide.pdf)
44. Weller, H. G., Tabor, G., Jasak, H., & Fureby, C. (1998). A tensorial approach to computational continuum mechanics using object-oriented techniques. *Computers in Physics*, 12(6), 620–631. <https://doi.org/10.1063/1.168744>
45. White, J. A., Chiaramonte, L., Ezzedine, S., Foxall, W., Hao, Y., et al. (2014). Geomechanical behavior of the reservoir and caprock system at the In Salah CO<sub>2</sub> storage project. *Proceedings of the National Academy of Sciences*, 111(24), 8747–8752. <https://doi.org/10.1073/pnas.1316465111>
46. Xie, M., Mayer, K. U., Claret, F., Alt-Epping, P., Jacques, D., et al. (2015). Implementation and evaluation of permeability-porosity and tortuosity-porosity relationships linked to mineral dissolution-precipitation. *Computational Geosciences*, 19(3), 655–671. <https://doi.org/10.1007/s10596-014-9458-3>
47. Xu, T., Apps, J. A., & Pruess, K. (2004). Numerical simulation of CO<sub>2</sub> disposal by mineral trapping in deep aquifers. *Applied Geochemistry*, 19(6), 917–936. <https://doi.org/10.1016/j.apgeochem.2003.11.003>
48. Xu, T., Pruess, K., Xu, T., & Pruess, K. (1998). Coupled modeling of non-isothermal multiphase flow, solute transport and reactive chemistry in porous and fractured media: 1. Model development and validation. <https://escholarship.org/uc/item/9p64p400>
49. Zhang, Y., Hu, B., Teng, Y., Tu, K., & Zhu, C. (2019). A library of BASIC scripts of reaction rates for geochemical modeling using phreeqc. *Computers & Geosciences*, 133, 104316. <https://doi.org/10.1016/j.cageo.2019.104316>
50. Zheng, S. (2021). Development of a fully integrated equation of state compositional hydraulic fracturing and reservoir simulator. The University of Texas Austin [Dissertation] <https://doi.org/10.26153/TSW/16954>